



On the relation between the planetary boundary layer height and in situ surface observations of atmospheric aerosol pollutants during spring in an urban area

Romanos Foskinis ^{a,b,c,i}, Maria I. Gini ^a, Panagiotis Kokkalis ^d, Evangelia Diapouli ^a, Stergios Vratolis ^a, Konstantinos Granakis ^{a,e}, Olga Zografou ^a, Mika Komppula ^f, Ville Vakkari ^{g,h}, Athanasios Nenes ^{c,i}, Alexandros Papayannis ^{b,i}, Konstantinos Eleftheriadis ^{a,*}

^a Environmental Radioactivity & Aerosol Tech. for atmospheric and climate impact Lab, INRATES, National Centre of Scientific Research "Demokritos", GR-15310 Ag. Paraskevi, Attiki, Greece

^b Laser Remote Sensing Unit, Physics Department, School of Applied Mathematics and Physical Sciences, National Technical University of Athens, GR-15780 Zografou, Greece

^c Center for Studies of Air Quality and Climate Change, Institute of Chemical Engineering Sciences, Foundation for Research and Technology Hellas, GR-26504 Patras, Greece

^d Department of Physics, Kuwait University, P.O. Box 5969, 13060 Safat, Kuwait

^e Climate and Climatic Change Group, Section of Environmental Physics and Meteorology, Department of Physics, National and Kapodistrian University of Athens, Athens GR-157 84, Greece

^f Finnish Meteorological Institute, FI-70211 Kuopio, Finland

^g Finnish Meteorological Institute, FI-00101 Helsinki, Finland

^h Atmospheric Chemistry Research Group, Chemical Resource Beneficiation, North-West University, Potchefstroom, South Africa

ⁱ Laboratory of Atmospheric Processes and their Impacts, School of Architecture, Civil & Environmental Engineering, École Polytechnique Fédérale de Lausanne, CH-1015 Lausanne, Switzerland

ARTICLE INFO

Keywords:

Planetary Boundary Layer
Remote Sensing
LiDAR
Atmospheric Aerosols

ABSTRACT

In this study we present the role of the Planetary Boundary Layer Height (PBLH) on the air pollutant concentrations measured at an urban background station at the megacity of Athens, Greece, an area characterized by complex topography. For this purpose, we utilized in situ measurements of aerosol number concentrations at different size bins (10–200 nm) $N_{10-200nm}$, (200–550 nm) $N_{200-550nm}$, equivalent Black Carbon (eBC), and wind speed data, for the period of May – July 2020. According to our analysis, both horizontal transport and vertical mixing and dispersion of air pollutants play a critical role in air quality. More precisely, PBLH is negatively correlated with aerosol concentration. The increase in the height of the Planetary Boundary Layer (PBL) favors a reduction in aerosol concentration, which, to some extent, compensates for the increase in aerosol load due to emission sources and horizontal transport from the city center. The horizontal advection process is related to the PBLH, since a deep PBL drives the advection, while a shallow PBL is characterized by weak horizontal wind velocities. On the other hand, under stagnant air mass conditions, when the PBL shrinks, the concentrations of air pollutants increase. On average, a 25% increase in the PBLH results in a 15% reduction in aerosol concentration, whereas a 15% reduction in the PBLH may result in a 10% increase in aerosol concentrations. Overall, $N_{10-200nm}$ particle concentrations increases, when air masses arrive from the S-NW sector (city center) due to traffic and vehicle emissions, while transport of continental pollution mixed with local and regional emissions along the Balkans-Aegean Sea axis, is originating from the NE axis under high wind speeds. The latter is more clearly recognized from aged aerosol components such as sulphate. Whereas, the $N_{200-550nm}$ and eBC showed increased concentration load under stagnant air mass conditions, independently of the wind direction.

* Corresponding author.

E-mail address: elefther@ipta.demokritos.gr (K. Eleftheriadis).

1. Introduction

The lowest part of the troposphere, called “Planetary Boundary Layer” (PBL), is directly linked to the surface, and is responsible for the energy and mass fluxes from the surface to the atmosphere (Stull, 1988). Most of the emitted aerosol particles and air pollutants from ground reside within this layer. It is well documented, that the atmospheric aerosols are produced by natural sources, anthropogenic activities, and atmospheric processes, while their lifetime varies from several hours for re-suspended coarse ($>1 \mu\text{m}$) dust to several days for fine ($<1 \mu\text{m}$) primary and secondary aerosols (soot, sulfate, etc.) (Eleftheriadis et al., 2006). The observed aerosol particle concentrations result from a combination of the emission dynamics, atmospheric processing, transport and dispersion within the PBL.

Lower tropospheric aerosol concentrations are directly influenced by anthropogenic emissions of primary particles, condensation of gaseous precursors of anthropogenic or natural origin, and natural sources, such as the sea and erodible soils (Seinfeld and Pandis, 2016).

Furthermore, aerosols also bear a strong impact on human health (Laden et al., 2006; Chalvatzaki et al., 2018; Stafoggia et al., 2017; WMO, 2022), air quality, and atmospheric visibility. Recent studies (Brook et al., 2010; Olstrup et al., 2019) have linked several respiratory and cardiovascular diseases, increased mortality, and decreased life expectancy (Liu et al., 2019; Lelieveld et al., 2020) with the increasing human exposure to high levels of fine and ultrafine particulates. Fine aerosols show significant contribution to detrimental health effects (Dockery and Pope, 1994; Ostro et al., 2006), while they act as carriers for toxic and mutagenic components (Beddows et al., 2004), and they are capable to penetrate cell membranes to cause intracellular damage (Salma et al., 2002; Li et al., 2003; Bell et al., 2009).

To improve our understanding on the aforementioned climatic effects, there is a strong need to measure several aerosol parameters (size distribution, chemical composition and concentration), both at ground level with in situ techniques (especially in the lowest part of the atmosphere, where aerosol concentrations are usually very high, mainly at highly populated urban areas) and aloft. For this purpose, we need to study the aerosol vertical distribution using active remote sensing techniques.

Another major aspect to mention here, is the variability of the planetary boundary layer top-height (PBLH). This variability is driven by the energy fluxes within the layer and changes the aerial volume where aerosols and other pollutants are dispersed therein, affecting the aerosol number concentration measured within the layer (Su et al., 2018; Jiang et al., 2022). On the other hand, Su et al. (2018) showed a strong negative correlation between the PBLH and the air pollutants concentrations. Under stagnant meteorological conditions, when the PBL becomes shallow, an increase of the concentration of the pre-existed aerosol is usually observed, an effect which is further amplified in valleys and basin areas surrounded by mountains (Papanikolaou et al., 2022). This seems to be a bidirectional relation, since according to Kokkalis et al. (2020) and Gini et al. (2022), aerosol intrusions inside the PBL, as well as the presence of transboundary transport aerosol layers above the PBL, may affect the top-height of the PBL and its evolution time during the day.

Our study aimed to investigate the effect of local air mass circulation and transport patterns on the aerosol load and its major chemical components, along with the PBLH diurnal cycle. To achieve this, we combined in situ measurements of key aerosol parameters with remote sensing techniques, to measure the horizontal component of wind, retrieve the PBLH and decouple the effect of the variability of PBLH on the air pollutant levels.

2. Methods and instrumentation

2.1. Experimental site

Athens Metropolitan Area (AMA) lies in the basin of the Attica peninsula, near the eastern Mediterranean coastline. The city hosts a densely populated urban area with about 3.8 million inhabitants in a 3000 km^2 , surface area, which is characterized by a variety of anthropogenic emissions, and a complex topography with about 2.5 million vehicles leading to heavy traffic conditions, having as a result important local aerosol emissions. Despite that Athens has been heavily deinindustrialized over the recent decades, there are still emissions from industrial processes and oil distilleries. The major industrial units currently located in AMA are two refineries, one fertilizer plant, two iron steel plants and one cement plant. These industrial plants are concentrated along the South West to North East axis, which includes the western quarters of the city and the central parts of Athens and Piraeus (Kalogridis et al., 2018). Furthermore, there are also about 100 medium sized industries, mainly in the domain of the food processing, the plastic and textile production (Katsoulis, 1996).

The measurements presented here have been conducted at the National Center for Scientific Research-Demokritos (DEM) station ($37.995^\circ \text{N}, 23.816^\circ \text{E}$, at 270 m a.s.l.). Station data are annually reported at the World Meteorological Organization (WMO) Global Atmospheric Watch (GAW) network and the Aerosol, Clouds and Trace Gases Research Infrastructure (ACTRIS) data centre (Laj et al., 2024). DEM is part of the PANhellenic infrastructure for Atmospheric Composition and climatE chAnge (PANACEA). The station is situated on the foot of Mount Hymettus in Agia Paraskevi, about 7 km northeast from the center of Athens (Vratolis et al., 2019) and is characterized as an urban background – suburban station, due to its proximity to the city-center. Therefore, it is influenced by fresh and aged traffic-related aerosol particles, especially when the prevailing wind has western (W) directions, and the regional background aerosol (Eleftheriadis et al., 2014; Kostenidou et al., 2015; Vratolis et al., 2019; Eleftheriadis et al., 2021).

2.2. Instrumentation

2.2.1. Wind lidar system (HALO)

A pulsed Doppler scanning lidar system (StreamLine Wind Pro model, HALO Photonics) emitting at $1.5 \mu\text{m}$ was deployed at the DEM site by the Finnish Meteorological Institute. The system was operated in the stare and vertical azimuth display (VAD) mode and mainly provided the vertical profiles of the radial wind (Henderson et al., 2005). The wavelength of the emitted laser beam is sensitive to backscatter from micron-sized aerosols. Thus, the measured wind velocity corresponds to the aerosol's velocity. The radial velocity of the scatterers is determined by the Doppler frequency shift of the backscattered pulse (Newsom and Krishnamurthy, 2020). Additionally, we used a filtering technique according to Barlow et al. (2011), to exclude the data with signal-to-noise (SNR) lower than -20 dB . We note that the noise measurement helps to correct for systematic variations in the noise floor of the Doppler spectrum. The range resolution of the wind measurements is 30 m, the temporal resolution is 2 s for the stare mode, the maximum measurement range is 2–3 km depending on the atmospheric aerosol load, giving an accuracy of the wind velocity better than $0.1\text{--}0.5 \text{ m s}^{-1}$. The VAD mode was operated in 70° elevation angle providing a conical scan every hour, with an angular resolution of 15° .

2.2.2. Aerosol microphysical and chemical parameters

The submicron aerosol size distributions are obtained with an Mobility Particle Size Spectrometer (MPSS), described in Vratolis et al. (2020). The MPSS provided size distributions every 5 min and was operated at an aerosol flow rate of 1 L per min and a sheath flow rate of 5 lpm, extending the measured particle size range from 10 to 550 nm. Data acquisition and analysis were performed using the non-commercial

TROPOS-MPSS data evaluation software (Wiedensohler et al., 2012). The instrument was also calibrated against a reference MPSS system at the World Calibration Centre for Aerosol Physics (WCCAP) in 2018 (Bousiotis et al., 2021), exhibiting a counting accuracy within 10% for the size range 30–550 nm against a reference system under controlled laboratory conditions (Wiedensohler et al., 2012).

The Aerosol mass and chemical composition monitor (ToF-ACSM, Aerodyne Inc.) measured the non-refractory submicron aerosol mass and chemical composition (sulfate, nitrate) in real-time (here, with 1 h time resolution), with a measurement uncertainty of the order of 30% (Budisulistiorini et al., 2014; Fröhlich et al., 2013). A collection efficiency factor $CE = 0.5$ (Zografou et al., 2022) was used to account for the fraction of the non-refractory particles that bounce off the vaporizer and are not detected.

The equivalent Black Carbon concentration (eBC) was obtained by on-line light-transmission measurements of ambient air samples marked on a filter tape at seven wavelengths (370, 470, 520, 590, 660, 880, and 950 nm), by means of an Aetahlometer (model AE33). After calculating the absorption coefficient it provides the eBC calculated of each wavelength (Petzold et al., 2013; Eleftheriadis et al., 2021). In this study we considered for eBC output using the wavelength at 880 nm. The inlet aerosol flows for all above instruments was, dried to a relative humidity lower than 40% by means of Nafion dryers.

2.3. Modelling and retrievals

2.3.1. Wind components retrieval using wind lidar system

Using the VAD scan technique (Browning and Wexler, 1968; Caya and Zawadzki, 1992) we obtain the horizontal components of the wind velocity: u , v , and w , along the north, east, and the vertical axis u , using the radial velocity (V_r) measurements, since the V_r value depends on the winds' four components, as follows:

$$V_r(r, \theta, \varphi) = u(r, \theta, \varphi) \sin\theta \cos\varphi + v(r, \theta, \varphi) \cos\theta \cos\varphi + w(r, \theta, \varphi) \sin\varphi \quad (1)$$

where r is the radial distance, θ is the azimuth angle from the north, and φ is the elevation angle ($\varphi = 70^\circ$).

Considering that the VAD mode of HALO provides measurements with a vertical resolution of 30 m and angular resolution of 15° for each time step, we calculated the average radial velocity within 3 spatial bins, giving a final vertical resolution of 100 m for each azimuth angle. Then, we applied a linear fit between the averaged radial velocities and the azimuth angles using Eq. 1 to determine the u , v components for each time step to be used to calculate the horizontal velocity V_h profile and the azimuthal wind direction V_θ angle profile, with the resolution given above.

2.3.2. PBLH retrieval using the wind lidar technique

According to Stull (1988), the PBL is defined as the lower part of the atmosphere that is directly influenced by the surface, and responds to surface forcing with a timescale of about an hour. Based on Tucker et al. (2009), Pearson et al. (2010), Barlow et al. (2011), Träumner et al. (2011), and Schween et al. (2014), in case of convex profiles (Kaimal et al., 1976), the PBLH can be estimated using a threshold technique on the standard deviation of vertical velocities (σ_w). In this study we used the vertical velocity data retrieved by HALO, to calculate the σ_w considering the surrounding data of ± 15 min interval for every 5 min and for every 30 m height layer. This 30 min time window, as pointed out by Schween et al. (2014), it is representative of convective plumes and of eddy fluxes, since the latter needs about 16 min to travel through a mixing layer of 1 km height (which is a typical height during day-hours) considering an average ascent speed of 1 m s^{-1} . So, this average window, is almost twice the life time of such a plume. Finally, we determined the PBLH as the first height where the value of σ_w falls below the threshold value of 0.20 m s^{-1} (Tucker et al., 2009). Moreover,

Schween et al. (2014) performed a sensitivity study showing that a change in threshold of $\pm 25\%$, corresponds to a $\pm 7\%$ changes in height.

2.3.3. Air mass cluster analysis

Carslaw et al. (2006) showed that, by using air mass cluster analysis we can categorize the in situ aerosol loads records, according to the local transport patterns namely the wind velocity and direction. One of the commonly used clustering techniques in atmospheric applications is the Partition Around Medoids (PAM) clustering. The PAM technique is quite similar to the k -means algorithm (Beddows et al., 2009; Carslaw and Beavers, 2013), and depends on the chosen number of clusters " k ", while the classifications of each datum into a cluster come up by minimizing the intra-partition Euclidian's distances, regarding each k -mean.

The partitioning method, initially, divides the aerosol data into k distinct clusters, and all data points are assigned to the nearest cluster centers. Then, the cluster centers are re-calculated as the centroids of the newly formed clusters and the data points are re-assigned to the nearest cluster centers that just re-calculated. This process is repeated until the clusters reach the minimum intra-partition distances. The goodness of the clustering can be determined by using the Silhouette coefficient (Rousseeuw, 1987), which shows which objects lie well within their cluster, and which ones are merely somewhere in between clusters. In our study, we used the PAM clustering partitioning to classify in clusters the $N_{10-200\text{nm}}$, and $N_{200-550\text{nm}}$ considering both of the day- and night-time samples, using the optimal k of each. The way to determine the optimal number of clusters is by gradually increasing the number of clusters " k " stepwise from 2 to 10, and recording the Silhouette coefficient (Rousseeuw, 1987). When the Silhouette coefficient reached a desirable high plateau, then this k is considered as optimal. In our case the results of the optimal k values of $N_{10-200\text{nm}}$, and $N_{200-550\text{nm}}$ were found 5 and 4, and 5 and 6 for the day-hours and night-hours samples, respectively. Therefore, we classified the aerosol data in clusters using the optimal k values of each sample.

2.3.4. Dynamic Box model approximation

Next, we will examine the role of the PLBH variability on the observed aerosol concentrations. Thus, we initially chose as a metric the $N_{200-550\text{nm}}$ concentrations considering that this fraction is not generally affected by primary fresh emissions. In addition, we examined together the $N_{10-200\text{nm}}$ and the eBC concentrations, since they both are highly influenced by the anthropogenic aerosol emissions.

According to Hanna et al. (1982) we can approach the physical system by considering the particle mass balance equation applied inside the PBL, described in terms of a square "box" control volume, the top/bottom surfaces of which correspond to the ground/PBLH, respectively. The horizontal transport of air inside the PBL is characterized through the vertical box boundaries, while the in situ measurements of pollutants concentration are used to characterize the aerosol concentrations and other process rates. The original mass balance equation can be given as:

$$\frac{\partial C_i}{\partial t} = \frac{Q_s}{H_{PBL}} - \frac{u(C_i - C_b)}{L} - \frac{1}{H_{PBL}} \frac{\partial H_{PBL}}{\partial t} (C_i - C_a) \quad (2)$$

where C_i is the pollutants concentration in particles cm^{-3} , Q_s is a term related to the sources, sinks, production, chemical dissolution and decomposition of the pollutant i , u is the mean air mass horizontal velocity in the box, H_{PBL} is the PBLH, the C_a and C_b are the concentrations above the box's top and the upwind background concentration of the pollutant i , respectively. L is the length of the box.

In our study, we considered an ideal box with a horizontal cross section of $1 \times 1 \text{ km}$ and a free moving non transparent cap at the vertical axis. The non-transparent cap means, that the term C_a can be considered equal to zero simplifying the equation. Following that, the equation still contains C_b and Q_s , which cannot be distinguished by solving Eq. 2 at the same time. To overcome this limitation, we considered the term which is related to the sources sinks, production, etc. very small and close to zero within the box ($Q_s = 0$) given the background location of the site. This

assumption can be balanced by increasing the contribution of the horizontal transported aerosol loads, i.e. the value of C_b . Since this study aims only to decouple the effect of the variability of PBLH and not to decouple the source and transport fraction, we can only investigate the third term, and consider as one term the combined effect of transport, local sources and sinks. Hence, Eq. 2 can be written in a differential form, as follows:

$$\frac{\Delta C_i}{\Delta t}(t) = \frac{C_i(t + \Delta t) - C_i(t - \Delta t)}{2\Delta t} \quad (3a)$$

$$\frac{\Delta H_{PBL}}{\Delta t}(t) = \frac{H_{PBL}(t + \Delta t) - H_{PBL}(t - \Delta t)}{2\Delta t} \quad (3b)$$

$$DC_i^{t+s}(t) = -\frac{u(t)(C_i(t) - C_b(t))}{L} \quad (3c)$$

$$DC_i^h(t) = -\frac{C_i(t)}{H_{PBL}(t)} \frac{\Delta H_{PBL}}{\Delta t}(t) \quad (3d)$$

$$DC_i(t) = DC_i^{t+s}(t) + DC_i^h(t) \quad (3e)$$

where Δt is the time resolution between each measurement of the timeseries, which is equal to 15 min, while the terms DC_i^{t+s} , DC_i^h are the decoupled variances of the aerosol concentrations within the control volume due to the horizontal transport, sources and sinks and the one related to the PBLH variation, respectively; the latter will be called from now on “PBLH enhancement”, of the pollutant i , where i corresponds to the $N_{10-200nm}$, $N_{200-550nm}$ and eBC concentrations, respectively. Finally, the term DC_i is the variance in time of the in situ measured aerosol concentration on each moment t . In this study the PBLH was estimated by using a threshold technique on the standard deviation of the vertical wind velocities (σ_w) within the PBL (Barlow et al., 2011; Schween et al., 2014) using the stare mode of HALO. Then, we decouple the effect of PBLH using a dynamic box algorithm approach based on Hanna et al. (1982) and Jiang et al. (2022) which manages the terms of sources within the box, and the horizontal transports through the box, considering a vertical dynamic non-transparent top boundary.

2.4. Methodology for data treatment and combined use of in situ and remote sensing data

To implement the objectives of our study we used a synergy of remote sensing and in situ measuring techniques. At first, we measured the horizontal components of the wind; speed (V_h) and direction (V_{dir}), by using a pulsed Doppler scanning lidar system (HALO) in the VAD mode (Henderson et al., 2005). Additionally, we used the measured aerosol size distribution, the non-refractory aerosol mass and chemical composition of the organic and inorganics components and the eBC , as indicative aerosol metrics respectively.

The size resolved aerosol number concentration was split in two fractions with diameters ranging between 10 and 200 nm and 200–550 nm. Particles within the size range 10–200 nm are associated with fresh emissions (contributing mainly within the range 15–60 nm), those within the size range of 60–90 nm are related to the traffic emissions, while particles related to condensational growth can be found in the whole range 10–550 nm (Vratolis et al., 2019). On the other hand, the aerosol particles within the range of 200–550 nm, correspond mainly to aged particles partly circulated in the broad Attica region over several hours/days and partly transported from distant areas (e.g. Mediterranean, the Balkans, western Europe). Therefore, the following discussion emphasizes on the mean aerosol number concentrations between 10 and 200 nm ($N_{10-200nm}$) and 200–550 nm ($N_{200-550nm}$). The eBC concentrations in the Athens Metropolitan Area (AMA) general range within 0.2–5 $\mu\text{g m}^{-3}$ and are associated with road traffic emissions (Kalogridis et al., 2018), while during the cold period they are enriched with residential emissions for domestic heating purposes. The particle number

concentration under the timescales considered here (~ 24 h) and the geographical domain can be considered as a passive tracer. This holds for the more aged particles $N_{200-550nm}$ and eBC , which is chemically conserved.

Using the ToF-ACSM instrument we measured the mass concentrations of sulfate (SO_4^{2-}), and nitrate (NO_3^-) particles. These components are being used for comparison, as major aerosol species but are known to be strongly affected by atmospheric chemistry. Then, we combined the V_h and V_{dir} values with the in situ aerosol data obtained from SMPS, ToF-ACSM, and AE33 into a common dataset, averaged on an hourly basis. Moreover, we divided the dataset into two groups: the first concerns the data obtained during the “day-hours” (between 07:00–23:00 LT), while the second is related to the data sampled during the “night-hours” (23:00–07:00 LT). Finally, we performed a cluster analysis using the probability approximation method (PAM) (see Section 2.3.3 Air mass cluster analysis) to determine the clusters of the in situ variables ($N_{10-200nm}$, $N_{200-550nm}$, SO_4^{2-} , NO_3^- , and eBC) with respect to the wind conditions, for each data group (day-hours and night-hours). Then, we correlated these clusters with the prevailing wind flows in the AMA.

In the second part of this paper, we examine the impact of PBLH’s variation on the concentrations of $N_{10-200nm}$, $N_{200-550nm}$ and eBC . In general, most of the surface emitted aerosols and air pollutants are trapped within the PBL, especially in the case of temperature inversions at the top of the PBL, which inhibit the aerosols to penetrate into the lower free troposphere. As mentioned previously, the PBLH is driven by the energy balance of the surface. Here, we consider any entrainment of aerosols at the interface of the PBL top to be relatively small.

Relevant studies (Su et al., 2018) have also shown a strong negative correlation between the PBLH and the air pollutants concentration at the surface, indicating that in the case of a shallow PBL, the total atmospheric volume within it, decreases and consequently, the particles concentration increase and vice versa.

In this study we used a dataset derived from air pollution measurements inside the AMA performed from 15 March to 2 July of 2020, including the COVID-19 lockdown period in Greece. In brief, during this period, starting on 11 March 2020, a series of mitigation measures against the spread of the COVID-19 pandemic were gradually implemented in Greece (Eleftheriadis et al., 2021). For instance, the operation of all educational institutions was suspended nationwide, two days later all commercial and social recreation activities were also suspended, except those related to basic needs (e.g. food supply, etc.); finally, from 22 March to 4 May, the lockdown measures were applied, including the restriction of all non-essential transportation throughout the country. It is well documented that the measures taken during the COVID-19 pandemic had a remarkable imprint on anthropogenic emissions by dramatically reducing traffic emissions (Eleftheriadis et al., 2021; Kokkalis et al., 2020), and by increasing residential emissions since there was a restriction on all non-essential travel throughout Greece and several European countries (Putaud et al., 2023), and the citizens had to stay indoors and make use of the residential heating on a continuous basis.

3. Results & discussion

3.1. Local transport pattern analysis

The orientation of the four surrounding mountains in the AMA are: Egaleo, Parnitha to the northwest, Penteli to the north and Hymettus to the east (c.f.

Fig. 1). This topography favors the formation of synoptic winds or the sea breeze cells following towards two directions, from the N-NE or SW (Kallos et al., 1993), respectively (see also section 2.1).

When a strong pressure gradient occurs over the Aegean Sea, then the N winds are linked with the AMA ventilation (Kallos et al., 1993). According to Diapouli et al. (2014) and Vratolis et al. (2019), the winds from the N sector are also related with transport of continental pollution

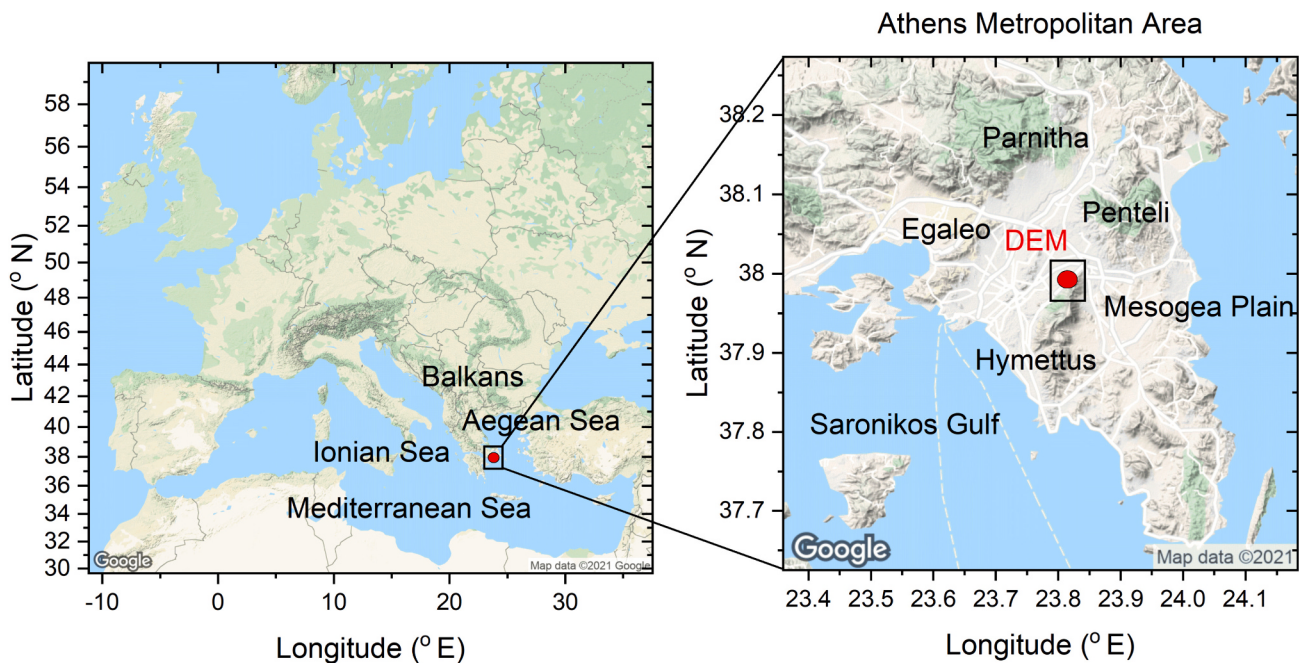


Fig. 1. Study area (left) and the sub-domain over the AMA (middle) marked by a red dot. (For interpretation of the references to color in this figure legend, the reader is referred to the web version of this article.)

mixed with local and marine emissions along the Balkans-Aegean Sea axis. These air masses usually reach the AMA region from the eastern side of Hymettus, while passing over the South Euboean Gulf and Mesogeia plain, transporting significant load of particles in the range of 10–200 nm (c.f. Fig. 2a) and increasing the SO_4^{2-} component (c.f. Fig. 2e). On the other hand, when a low-pressure gradient over the Central Mediterranean or Ionian Sea occurs, then S & SW winds are developed over AMA, usually related to Saharan dust transport events

over the Athens basin (Soupiona et al., 2019), while air pollutants ($N_{10-200nm}$ & eBC) produced in the densely populated part of the Athens basin are also transported towards DEM station (Kalogridis et al., 2018; Gini et al., 2022). As AMA is surrounded by mountains except from its southwestern side which is an extended opening towards the Saronikos Gulf, the sea breeze cells can be developed under relatively weak synoptic flow conditions over Greece, affecting the ventilation of AMA. In general, the sea-breeze tends to stratify the atmosphere above the city,

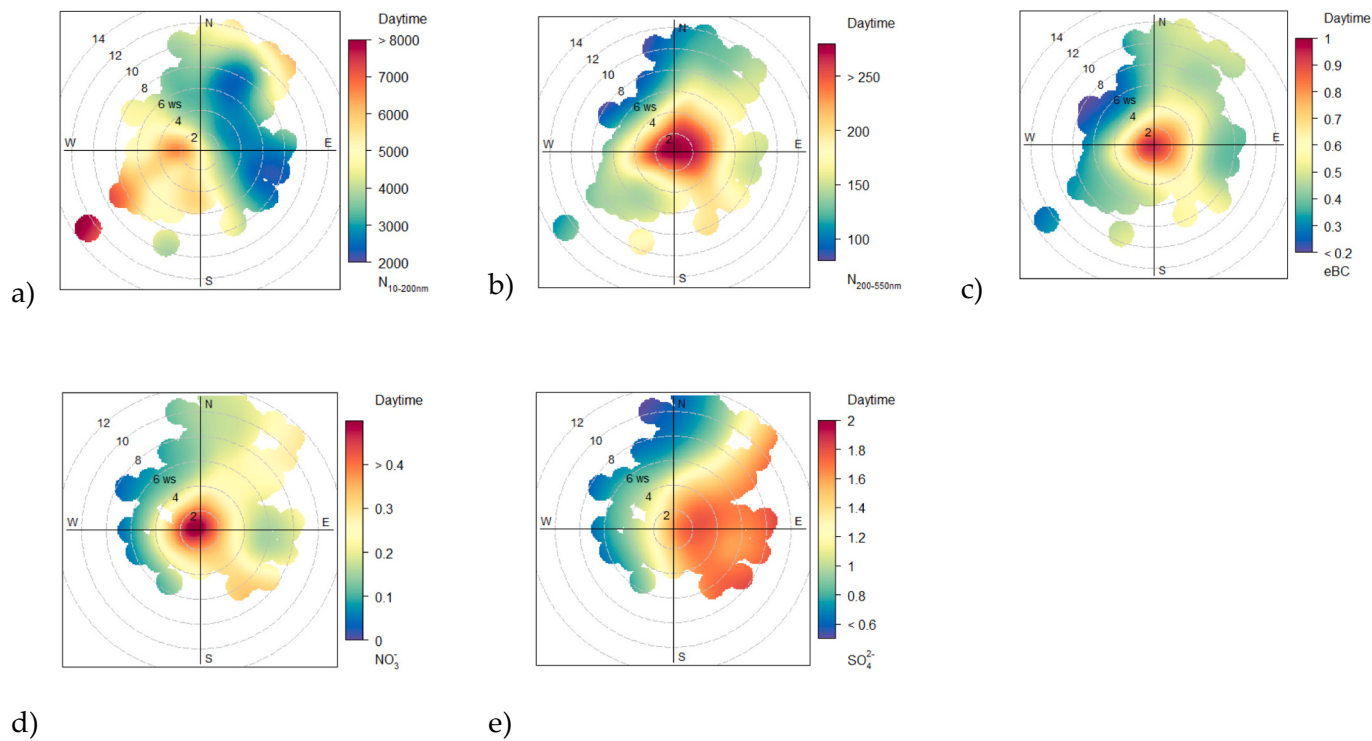


Fig. 2. Wind polar plots of (a) $N_{10-200nm}$ [cm $^{-3}$], (b) $N_{200-550nm}$ [cm $^{-3}$], (c) eBC [$\mu\text{g m}^{-3}$], (d) NO_3^- [$\mu\text{g m}^{-3}$] and (e) SO_4^{2-} [$\mu\text{g m}^{-3}$] during the daytime, respectively. The radial distance from the middle of the plot corresponds to the wind speed, while the color-scale corresponds to the concentration of each pollutant.

trapping air pollutants in a relatively small height above ground (Kallas et al., 1993), while under stagnant atmospheric conditions, locally-emitted anthropogenic aerosols dominate inside the PBL (Kalogridis et al., 2018).

In Fig. 2a, a significant increase of concentrations in the $N_{10-200nm}$ mode particles is observed over the AMA with wind flows within the S – NW sectors, due to the locally formed sea breeze cell. This is because the S – NW sector corresponds to the city center, and as a result, this sector is the highest contributor of aerosol load to our measurement station. At the same time along this axis and during periods with strong sea breeze, recirculation of the pollutants along the NE–SW axis is dominant (Kallas et al., 1993; Kalabokas et al., 1999; Diapouli et al., 2017a, 2017b). Another sea breeze cell is formed over the Mesogeia plain at the eastern side of Hymettus and blows mainly from SE to W/NW (during daytime) and from W/NW to SE (during the nighttime) (Kallas et al., 1993). The Mesogeia plain is generally less populated, and also with lower vehicular traffic, compared to the AMA. Therefore, when low winds occur, relative “clean” air masses are transported over the DEM site, characterized by low particle number concentrations in both size ranges (10–200 nm and 200–550 nm) (Kostenidou et al., 2015; Vratolis et al., 2019).

On the other hand, we used the SO_4^{2-} concentrations, as a tracer for regional anthropogenic aerosol and continental pollution, since there are no significant sources of SO_4^{2-} within AMA (Zografou et al., 2022). In Fig. 2e we observe higher SO_4^{2-} concentrations when the wind flows within the NE–SE sector (Diapouli et al., 2014; Vratolis et al., 2019). This pattern remains the same during the nighttime conditions (c.f. Fig. 2e). According to Amanatidis et al. (1992), the katabatic flows inside a basin like AMA surrounded by mountains are very important, since they enhance the air pollution episodes. When the katabatic flows occur, the pre-existed and emitted aerosols within the PBL, are trapped in poor pollutant dilution and dispersion along low winds and temperature

inversion, and as a result, the pollution episodes become more intense. Additionally, Flocas et al. (1998) found the same direction for the katabatic winds, a finding indicating that the increase in the particle number concentration we observe, originates from particle layers aloft transported by the katabatic flow regime.

This can be seen in Fig. 3b, and c, in which an increment of the $N_{200-550nm}$ and the eBC concentrations is observed when the winds blow within the sectoral range 130°–190°. As a result, the air masses from the mount Hymettus are brought over the station lowering the nocturnal PBLH, and occasionally increasing the particle number concentration (Flocas et al., 1998).

When stagnant conditions occur during nighttime, then the observed $N_{200-550nm}$, eBC, and the NO_3^- concentrations correspond to local emissions without a strong contribution on the aerosol load (c.f. Fig. 3c, d, and e).

3.2. Clustering of local transport patterns

Moreover, for the day- and night- time data series of $N_{10-200nm}$, and $N_{200-550nm}$, we performed a cluster analysis in order to group the data with respect to the aerosol load, the wind direction and speed. During this process we can identify an optimum number of clusters (sectors), so that the aerosol observations within each sector correspond to similar (wind speed and direction) conditions.

As mentioned before in this study we used the PAM clustering, while the number of the sectors was estimated by using the optimization technique of selection of the optimal number of clusters (see Section 2.3.3 Air mass cluster analysis).

Regarding the daytime periods, the $N_{10-200nm}$ and $N_{200-550nm}$ concentrations can be clustered into five and four sectors (c.f. Fig. 4a, b); for ultrafine and accumulation mode particles, respectively (see Fig. 4).

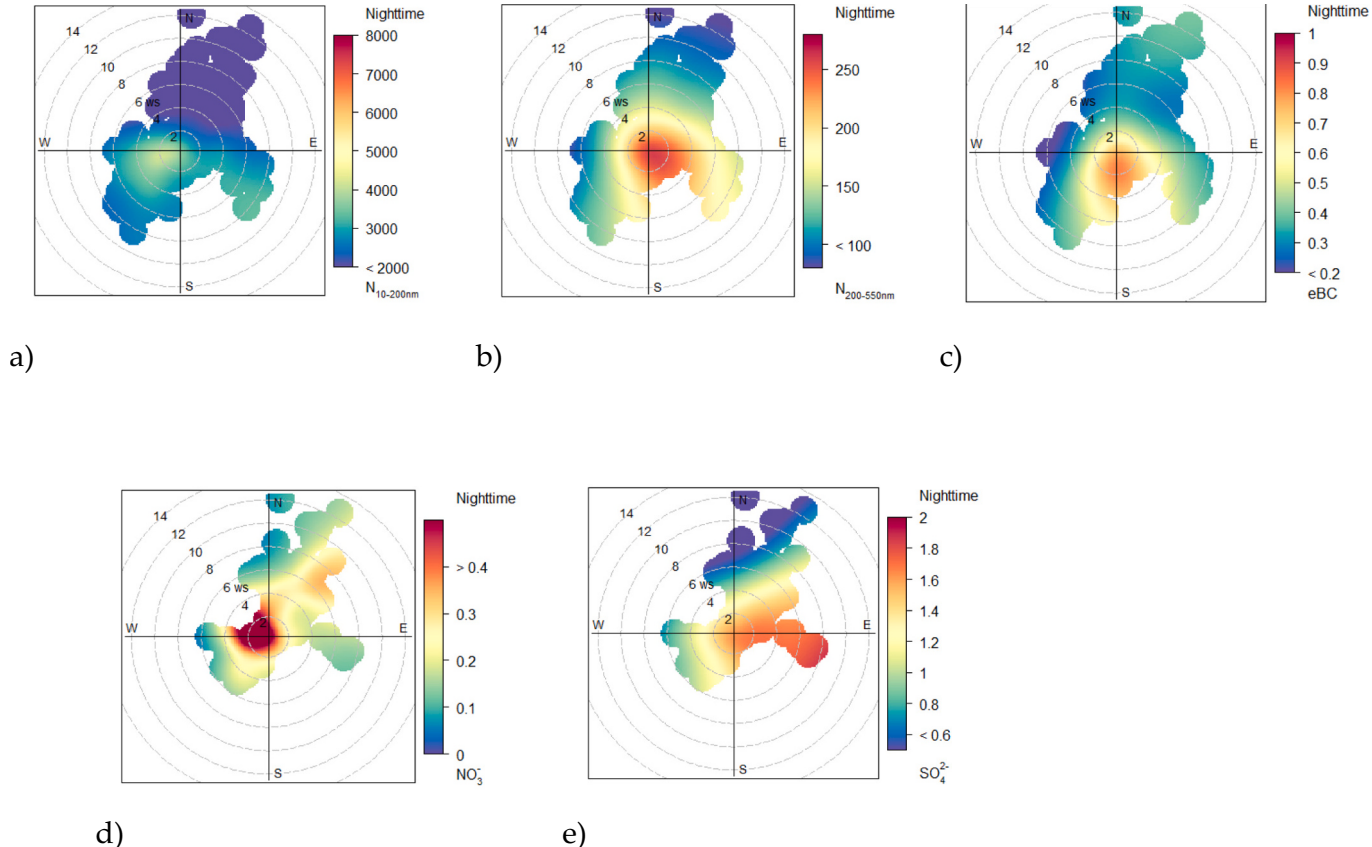
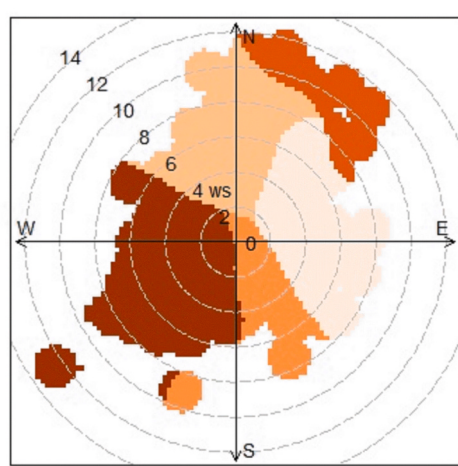
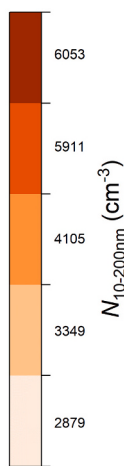


Fig. 3. Wind polar plots of (a) $N_{10-200nm}$ [cm^{-3}], (b) $N_{200-550nm}$ [cm^{-3}], (c) eBC [$\mu\text{g m}^{-3}$], (d) NO_3^- [$\mu\text{g m}^{-3}$] and (e) SO_4^{2-} [$\mu\text{g m}^{-3}$] during the night-hours, respectively. The radial distance from the middle of the plot corresponds to the wind speed, while the color-scale corresponds to the concentration of each pollutant.

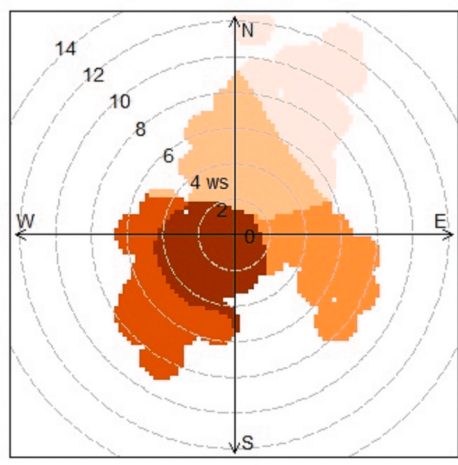
Daytime



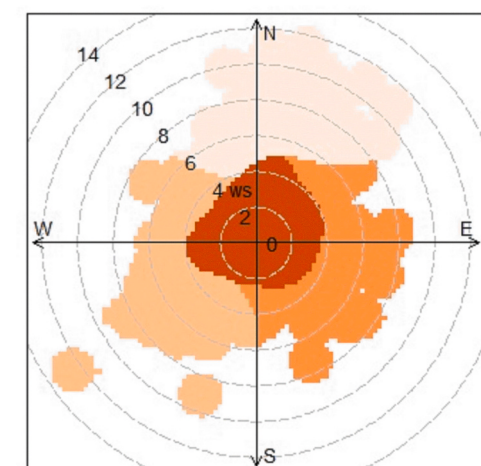
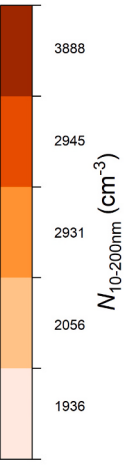
a)



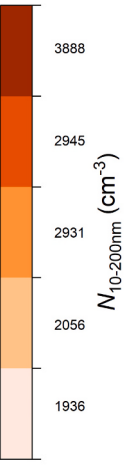
Nighttime



c)



b)



d)

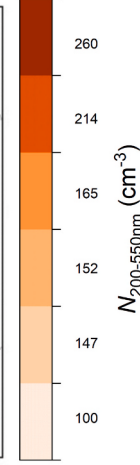


Fig. 4. Clustering results of $N_{10-200\text{nm}}$ and $N_{200-550\text{nm}}$ based on aerosol load in respect of the prevailing meteorological conditions for the day- and night- hour samples, respectively. Here the color-tone of each cluster indicates higher mean concentrations when the color becomes darker.

Thus, the main clusters were observed within the following sectors: the NE-SE sector, which corresponds to a residential or parkland area at the lee side of Hymettus with particle number dense aerosol sources, with the exception of the fast traffic Athens Ring-road (Figs. 4a, b). More specifically Fig. 4a presents the lowest aerosol concentrations values in average ($2879 \pm 1832 \text{ cm}^{-3}$ and $157 \pm 78 \text{ cm}^{-3}$ for ultrafine and accumulation mode particles, respectively); the NW-NE sector which is characterized by a densely populated urban/suburban area with typical local traffic emissions, has slightly high values on average ($3349 \pm 2095 \text{ cm}^{-3}$ and $204 \pm 127 \text{ cm}^{-3}$ for ultrafine and accumulation mode particles, respectively); the S-NW sector in which, the freshly emitted aerosol particles from traffic are transported from the major AMA urban and city-center sectors towards our experimental site, driven by the synoptic S winds or the sea breeze from the Saronikos Gulf. In this case, we found the highest aerosol loads ($6053 \pm 3784 \text{ cm}^{-3}$ and $171 \pm 123 \text{ cm}^{-3}$ in ultrafine and accumulation mode particles, respectively); Finally, a narrow sector starting from the lee side of Hymettus to the SE-S direction, displayed occasional events of a slightly high load of ultrafine mode particles, equal to $4105 \pm 1705 \text{ cm}^{-3}$. Moreover, in the case of the ultrafine mode particles, we found even more increased values on average equal to $5911 \pm 3252 \text{ cm}^{-3}$ within the N-NE sector, where windy conditions frequently occur. Usually, this is a preferred

pattern for long-range transported continental pollution intrusions along the Balkans-Aegean Sea axis (Diapouli et al., 2014; Vratolis et al., 2019). Finally, one extra sector has been found in the case of accumulation mode particles which corresponds to the local emissions during stagnant conditions (valid when the wind speed is below 4 m s^{-1}). In total, the local aerosol emissions were estimated to appear equal to $269 \pm 153 \text{ cm}^{-3}$.

Concerning the nighttime periods the $N_{10-200\text{nm}}$ and $N_{200-550\text{nm}}$ concentrations, they can be clustered into five and six sectors (c.f. Fig. 4c, d); for ultrafine and accumulation mode particles, respectively (see Fig. 4), similarly to the daytime analysis the major aerosol concentrations were observed within the following sectors: the sector which is associated to local emissions during stagnant conditions (for wind speeds $< 4 \text{ m s}^{-1}$) in for both ultrafine ($3888 \pm 1970 \text{ cm}^{-3}$) and accumulation ($260 \pm 160 \text{ cm}^{-3}$) mode particles; the S-NW sector, which is affected by aerosol emissions from the city-center ($2945 \pm 1054 \text{ cm}^{-3}$ and $152 \pm 94 \text{ cm}^{-3}$); the NE and SE sectors are now associated with the katabatic flows from Hymettus, where we found an increase in the average aerosol load ($2931 \pm 1770 \text{ cm}^{-3}$ and $214 \pm 152 \text{ cm}^{-3}$ for wind speeds over 4 m s^{-1}) most probably originating from decoupled aerosol layers aloft (Papayannis and Balis, 1998); the NW, N and NE sectors (for the fine mode particles) are unified showing concentrations of $2056 \pm 1041 \text{ cm}^{-3}$, while in the

case of accumulation mode particles this sector is divided into NW-N and N-NE sectors, respectively ($147 \pm 92 \text{ cm}^{-3}$ and $165 \pm 99 \text{ cm}^{-3}$); and finally, the N-NE sector when wind speeds $>6 \text{ m s}^{-1}$ ($1936 \pm 1508 \text{ cm}^{-3}$ and $100 \pm 49 \text{ cm}^{-3}$).

The overall assessment of the 3D air flow around DEM station reveals a strong influence of mainly stagnant conditions being responsible for the high concentrations observed for aerosol metrics like particle number and *eBC*. This indicates that sources within the Athens valley are the main influence for the site. It is observed that metrics related to fresh emissions ($N_{10-200\text{nm}}$, *eBC*) display a tendency to arrive from the W/SW sector (city center and main urban area) at higher wind speeds, while SO_4 which is characteristic of regional distant sources tend to arrive from the eastern sector outside the Athens valley rather than the west sector.

3.3. PBLH decoupling on aerosol monitoring

3.3.1. Case Study Analysis (9 May 2020)

In this section we will analyze the diurnal evolution of the PBLH during the case study of 9 May 2020. At first, we present in Fig. 5a, b, c, the spatio-temporal evolution of the range-corrected lidar signal (RCS), w and σ_w (based on the methodology described in Section 2), respectively, from ground up to 3 km height, where the red dots denote the PBLH. As noted in Section 2.4.2, by applying the σ_w threshold technique, the PBLH can be estimated, where σ_w takes values $>0.2 \text{ m s}^{-1}$.

In Fig. 5a we observe that the PBLH is increasing during daytime, reaching its maximum height of $\sim 2000 \text{ m a.g.l.}$ at $\sim 15:00 \text{ LT}$. During its diurnal evolution (09:00–20:00 LT) the PBL contains well mixed aerosols, as a result of strong air mass updrafts (the positive part of the

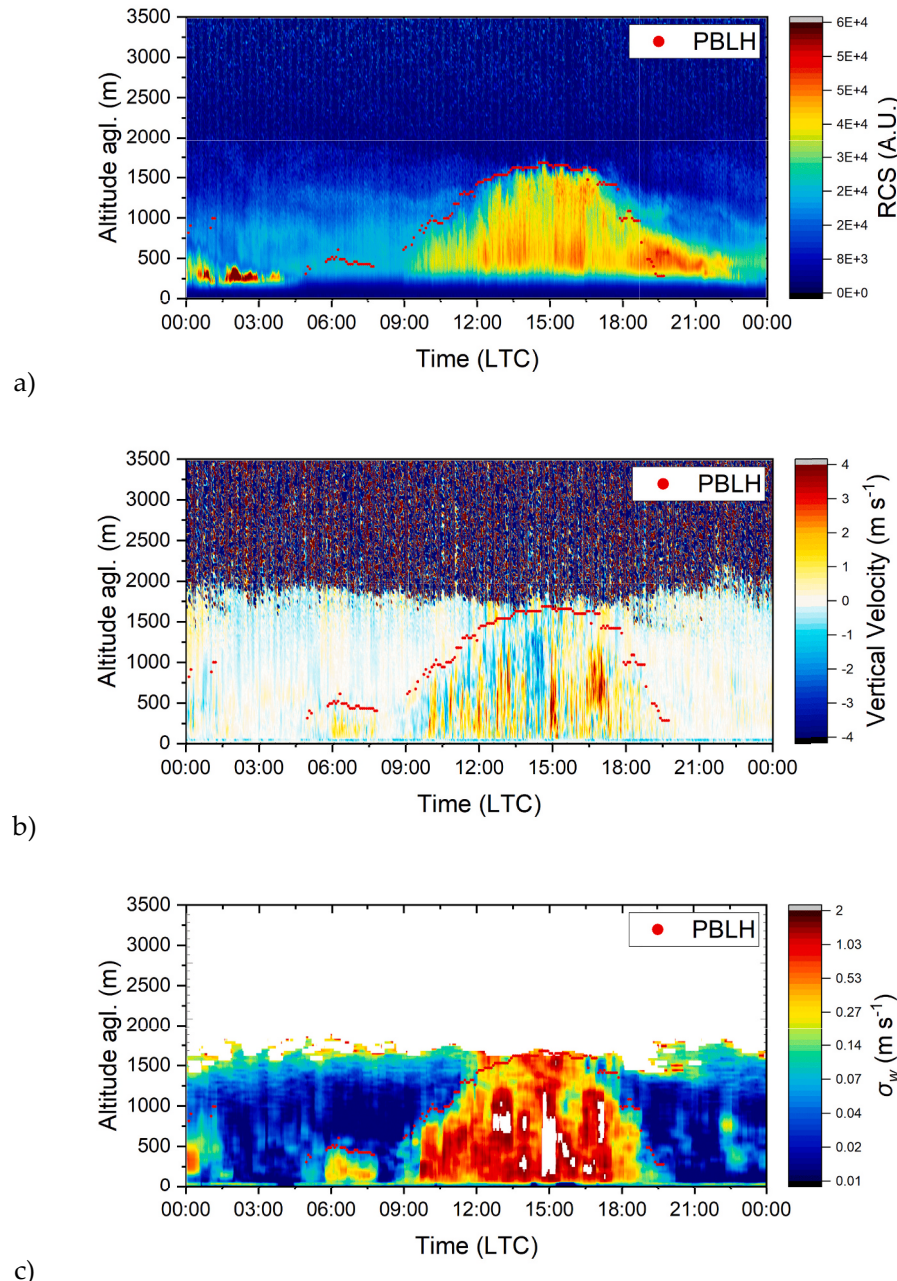


Fig. 5. Spatio-temporal evolution of (a) RCS in arbitrary units, (b) vertical velocities in m s^{-1} , and (c) σ_w in m s^{-1} of 9-May 2020, respectively. The red dots indicate the temporal evolution of the PBLH. LTC stands for Local Time Zone. (For interpretation of the references to color in this figure legend, the reader is referred to the web version of this article.)

vertical velocities). More specifically, after 09:00 LT the ground surface temperature starts increasing due to solar heating, producing a positive (upward) radiative flux. Thus, the air parcels located close to the ground absorb part of that energy and get warmer and, finally, a convective process starts following the buoyancy rules. Therefore, heat is transferred vertically, from lower to higher altitudes inside the PBL. This vertical motion forces the nearby air parcels to fill the gap near ground, thus, increasing the turbulence. Following the daily cycle, the development of the PBLH continues as long as the net radiative flux is positive. When the sun is on zenith ($\sim 15:00$ LT), the solar net flux together with the PBLH reach their maximum values, as the PBLH does. Later, during the afternoon and the sunset, the PBLH decreases gradually since the heat transfer from ground reduces, and the turbulence becomes weaker.

Furthermore, by solving Eq. 3 for each aerosol cluster, we calculated the decoupled DC_i^{t+s} and DC_i^h values along the DC_i^{obs} for the $N_{10-200nm}$, $N_{200-500nm}$, and eBC values, respectively. The diurnal evolution of DC_i^{t+s} , DC_i^h , DC_i^{obs} , $N_{10-200nm}$, $N_{200-500nm}$, and eBC is presented in Fig. 6a, b and c, respectively, along with the PBLH values. Finally, the wind rose plot

presented in Fig. 6d, shows which flow direction contributes more to the aerosol advection inside the PBL.

We note, here, that the positive fraction of DC_i^{t+s} indicates advection of air masses (and pollutants), while the negative values indicate dilution and removal processes. The horizontal advection process is also related to the PBLH, since a deep PBL drives the advection, while a shallow PBL is characterized by weak horizontal wind velocities, along with frictional drag effects close to the surface. Indeed, this can be seen in Fig. 6b and d, between 10:00–15:00 LT, as the PBL is developing and horizontal wind velocities are increasing, advecting freshly emitted particles from the city's center towards our measurement site. As a result, the DC_i^{t+s} values become positive, for all particles (ultrafine, accumulation mode particles and eBC). Meanwhile, the inflation of the PBL has a negative impact on the DC_i^h values, due to the increase in the total atmospheric volume below the PBL. However, despite this decrease, the DC_i^{t+s} dominates over the DC_i^h and results to an overall increase in concentrations, for both ultrafine, accumulation mode particles, as well as the eBC .

Once the PBL stops growing (15:00–17:00 LT), the wind flow

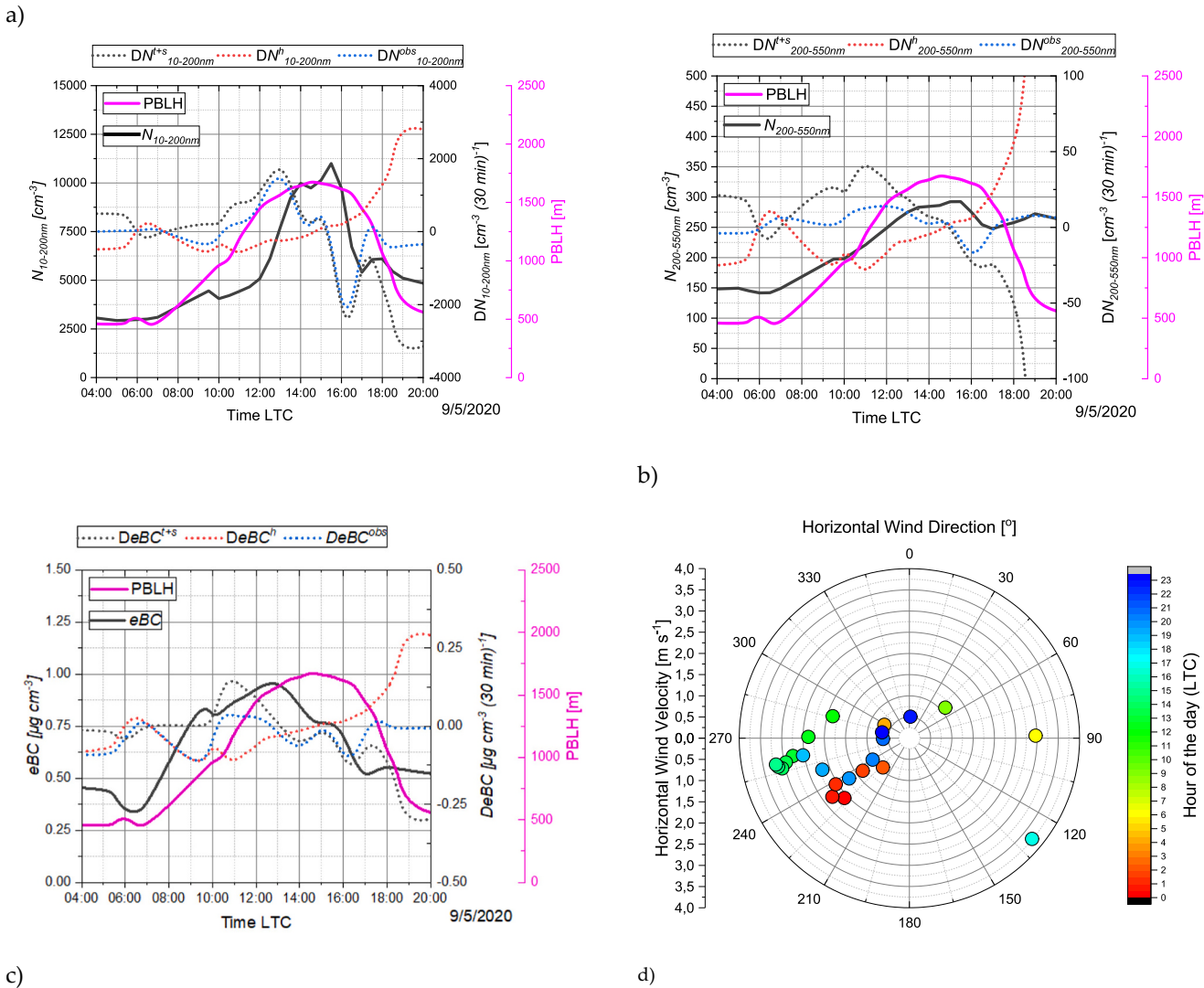


Fig. 6. Diurnal evolution of a) $N_{10-200nm}$, b) $N_{200-500nm}$, and c) eBC concentrations (9 May 2020), along with the decoupled evolutions of horizontal transport or source/sinks fraction and the PBLH enhancement fraction. The black line corresponds to the concentration of the pollutant (left axis), the dot lines correspond on the right axis to the decoupled concentration rate of change of each pollutant, where the horizontal transport or source/sinks fraction is in black, the PBLH enhancement is in red, the measured change in blue. The magenta line corresponds to the second axis on the right and presents the PBLH. d) The temporal evolution of the wind velocity and direction with respect to local time, for the case of 9 May 2020. (For interpretation of the references to color in this figure legend, the reader is referred to the web version of this article.)

changes from *W* to *SE* direction, ventilating the site and transferring purer air masses towards our site. This causes a reduction in the aerosol load (both in ultrafine, accumulation mode particles, and the *eBC* concentrations). Finally, from 17:00 to 20:00 LT, the PBL rapidly shrinks down, leading to a positive DC_i^h enhancement. Overall, the observed aerosol concentrations increase and stabilize to a certain level, indicating an enhancement from the suppression of PBLH, without any significant transport from sources.

The PBL diurnal variation appears to have a significant impact on aerosol concentrations observed at this background location and this can be quantitatively demonstrated by the present study. Although it does not alter the strong features of the diurnal variability of representative aerosol pollutant metrics, some characteristic behavior of the rate of change in concentrations is observed. More specifically, the increase of PBLH in the morning hours advects fresh pollutants at a rate which would be higher if not diluted by the increased PBLH. This is more pronounced for fresh particle emissions and *eBC*. In the evening hours concentration levels are retained to higher levels or display peaks, while they would otherwise decline sharply.

3.3.2. Diurnal variations of pollutants inside the PBL

In this section, we used the same methodology described for the case study above, to the entire period of measurements. In Fig. 7a, b and c, we present the diurnal variations of the same parameters (as in Fig. 6) along with their decoupled fractions, for the period 15 March to 2 July of 2020. Here the colored-shadows correspond to the standard deviation of each variable calculated for each hour, respectively.

Based on Fig. 7a, we can observe the diurnal cycles of $N_{10-200nm}$ and PBL. The diurnal cycle of $N_{10-200nm}$ is shown to have a clear dependence on the anthropogenic emissions, since the cycle matches to vehicular traffic pattern within the AMA. The average $N_{10-200nm}$ concentrations were found to be equal to 2500 cm^{-3} , 8750 cm^{-3} , and 3750 cm^{-3} at 06:00, 13:00, and 19:00 LT, respectively. In contrast, the $N_{200-500nm}$ concentrations did not show a strong diurnal cycle, ranging on average between 200 and 300 cm^{-3} . Additionally, the *eBC* concentrations exhibited two peaks: the first peak (06:00–10:00 LT) was related to vehicular traffic, while the second peak (18:00–23:00 LT) was related to the residential heating emissions in agreement with a study conducted in the same period (Eleftheriadis et al., 2021). Throughout the studied

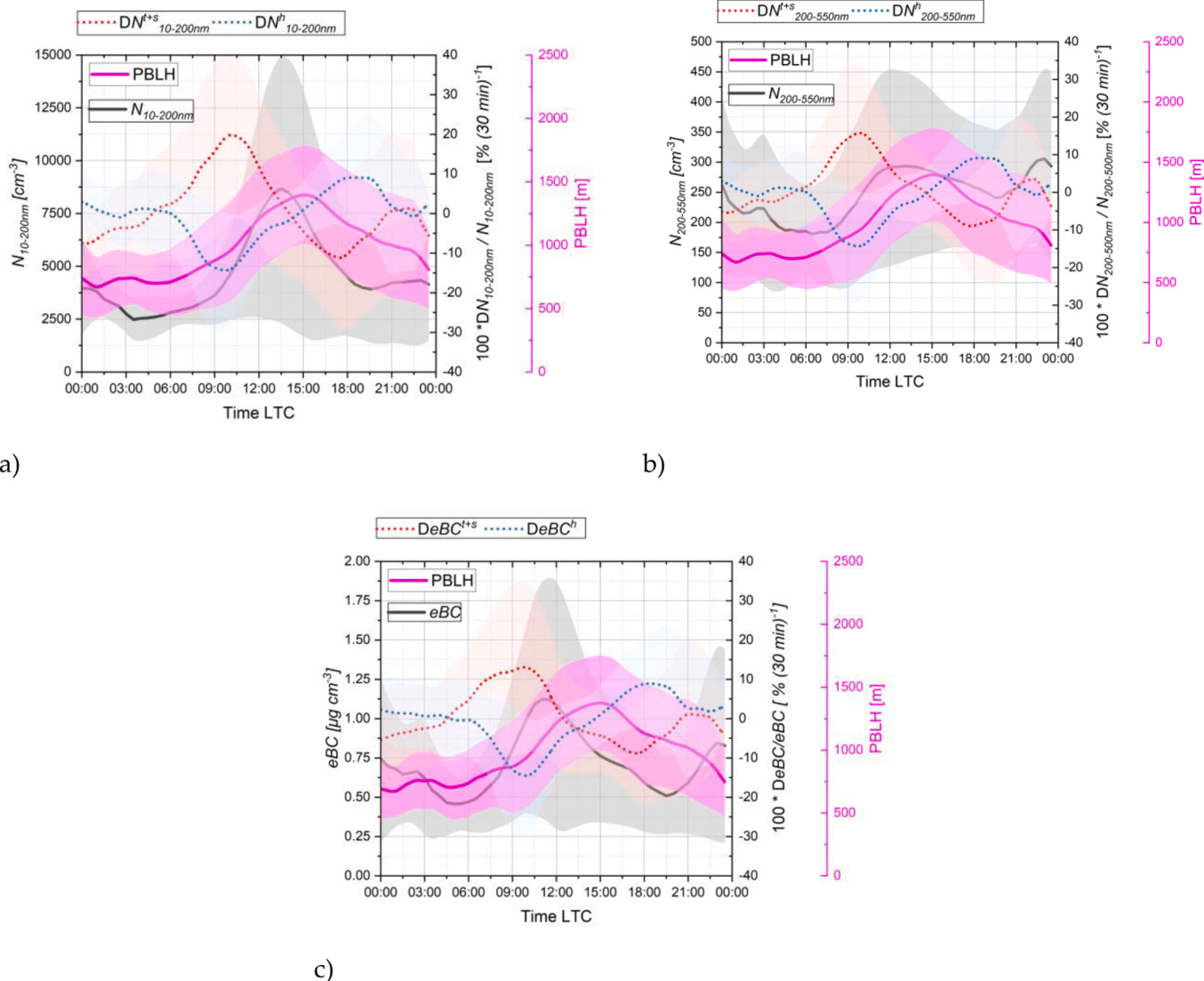


Fig. 7. Diurnal evolution of a) $N_{10-200nm}$, b) $N_{200-500nm}$, and c) *eBC* concentrations, along with the decoupled evolutions of horizontal transport or source/sinks fraction and the PBLH enhancement fraction. The black line corresponds to the concentration of the pollutant (left axis), the dot lines correspond on the right axis to the decoupled concentration change of each pollutant, where the horizontal transport or source/sinks fraction is in black, the PBLH enhancement is in red, the measured change in blue. The magenta line corresponds to the second axis on the right and presents the PBLH. (For interpretation of the references to color in this figure legend, the reader is referred to the web version of this article.)

period, the PBLH revealed a clear diurnal cycle, fluctuating between 500 and 1200 m agl. (06:00 to 21:00 LT).

In general, the decoupled DN_i^{t+s} and DN_i^h fractions were found to be anticorrelated to each other. This means that when the PBLH is growing, it promotes the air mass advection, leading to an increase in DN_i^{t+s} values. At the same time, the relevant aerosol concentrations are reduced, as the atmospheric volume in which they are embedded increases (i.e. vice versa decrease of the DN_i^h values compared to DN_i^{t+s} ones). Consequently, the observed rate of change (DN_i^{obs}) is fluctuating between the DN_i^h and DN_i^{t+s} values.

Throughout this study it is demonstrated that during the transition periods of rising or contracting PBL a rate of change in the range of 10–20% is dynamically induced and modulates the concentration levels of aerosol pollutants. In Fig. 7 this corresponds to different levels based on the relative concentration of each specie. However, if one looks at the change induced by the rate of change of PBL height alone all aerosol parameters are affected in the same way, behaving like passive tracers at the given time resolution (Fig. S1). The effect is not pronounced to the point of altering the diurnal pattern related to the urban emission sources but must be taken into account for interpreting the temporal evolution of observed concentration levels. Overall, the expansion of PBLH in the morning till midday does not induce the expected dilution and reduction in concentration levels since the major emission sources like traffic are increasing and combined with horizontal transport or stagnant conditions provide an observed increase in concentrations, while in the afternoon and evening concentrations are maintained or decrease at a lesser rate despite the decline of emissions (with the exception of residential heating becoming evident in the case of eBC at the late hours).

4. Conclusions

The local transport patterns of fresh and aged particles, as well as their diurnal variations and their relation to the boundary layer top height, are analyzed and discussed here. For the implementation of the study, we utilized measurements of horizontal wind speed, aerosol size distribution, and chemical composition, using both remote sensing and in situ techniques during the time period from March 15th to July 2nd, 2020, over the megacity Athens, Greece.

According to our findings, the combination of topography and atmospheric dynamics plays an important role in the local ventilation and air quality conditions. More precisely, in the Athens valley background conditions at DEM station, the aerosol particle concentration increases significantly in the S-NW sector due to traffic and vehicle emissions ($6053 \pm 3784 \text{ cm}^{-3}$ and $171 \pm 123 \text{ cm}^{-3}$ in ultrafine and accumulation mode particles, respectively), as well as during windy conditions from the N-NE axis in case of ultrafine particles ($5911 \pm 3252 \text{ cm}^{-3}$). Moderate wind flows from NE-SE axis are mostly related to regional background air masses from the Mesogeia plain ($2879 \pm 1832 \text{ cm}^{-3}$ and $204 \pm 127 \text{ cm}^{-3}$ for ultrafine and accumulation mode particles). Using the SO_4^{2-} as a tracer, we identified the long-range transport, as it is mostly derived from and continental pollution and shipping emissions. During nighttime, we found that the katabatic flows from Hymettus Mountain may either provide background clean air from higher altitudes, while occasionally transfer pollutants decoupled to higher layers, enhancing pollution episodes, while during stagnant conditions this effect becomes more intense ($2931 \pm 1770 \text{ cm}^{-3}$ and $214 \pm 152 \text{ cm}^{-3}$ when wind speed $>4 \text{ m s}^{-1}$).

Moreover, the role of PBLH variation on the measured aerosol load is also examined in this study. The estimation of PBLH was achieved using a threshold technique and then a dynamic box approach was used to decouple the effect of PBLH on the concentrations of pollutants (i.e. $N_{10-200\text{nm}}$, $N_{200-500\text{nm}}$, and eBC).

Our analysis reveals that the variation of PBL height has a quantitative effect on aerosol concentrations observed at the ground. This is because any change in the aerosol concentration is partially related to

changes in sources or sinks emissions, horizontal transport effects and the variance of the height of the PBL. It is observed that for aerosol pollutants with different sources and diurnal patterns, the PBLH diurnal variability combined with horizontal transport patterns add extra features in their observed concentrations. Most striking feature is the peak concentrations to appear later in the day (around noon).

The significance of our results, demonstrate the importance of considering PBLH variations in understanding the impact of pollutants and their sources on air quality, especially in urban areas of complex topography. The methodology described in the study can be applied to other regions with similar conditions to estimate PBLH and its impact on air quality.

Author contributions

Conceptualization, R.F., K.E.; methodology, R.F., K.E., M.I.G and P.K.; data analysis, R.F., M.I.G., E.D, S.V., K.G., and V.V.; model simulations, RF; investigation R.F., A.P., and P.K; writing—original draft preparation, R.F., K.E., A.P., M.I.G, and P.K.; review and editing, R.F., A. N., A.P., E.D, K.E., M.I.G., M.K., and V.V.; visualization, R.F.; supervision, K.E., A.P. and P.K.; All authors have read and agreed to the published version of the manuscript.

Funding

This research was funded by the General Secretariat of Research and Innovation 105658/17-10-2019 in the framework of support of the research program “National Research Network for climate change and its effects” While, part of this work was financed by the Basic Research Program, NTUA (PEVE) under contract PEVE0011/2021.

CRediT authorship contribution statement

Romanos Foskinis: Writing – original draft, Validation, Methodology, Formal analysis, Data curation, Conceptualization. **Maria I. Gini:** Writing – review & editing, Writing – original draft, Methodology, Investigation, Formal analysis, Data curation. **Panagiotis Kokkalis:** Writing – review & editing, Writing – original draft, Supervision, Methodology, Investigation. **Evangelia Diapouli:** Writing – review & editing, Formal analysis, Data curation. **Stergios Vratolis:** Formal analysis, Data curation. **Olga Zografou:** Formal analysis, Data curation. **Mika Komppula:** Writing – review & editing. **Ville Vakkari:** Writing – review & editing, Formal analysis, Data curation. **Athanassios Nenes:** Writing – review & editing, Validation. **Alexandros Papayannis:** Writing – review & editing, Writing – original draft, Supervision, Investigation. **Konstantinos Eleftheriadis:** Formal analysis, Data curation.

Declaration of Competing Interest

The authors declare the following financial interests/personal relationships which may be considered as potential competing interests:

Romanos Foskinis reports financial support was provided by General Secretariat of Research and Innovation. If there are other authors, they declare that they have no known competing financial interests or personal relationships that could have appeared to influence the work reported in this paper.

Data availability

Data will be made available on request.

Acknowledgments

The authors acknowledge support by the project “PANhellenic infrastructure for Atmospheric Composition and climatE change” (MIS

5021516) which is implemented under the Action “Reinforcement of the Research and Innovation Infrastructure”, funded by the Operational Programme “Competitiveness, Entrepreneurship and Innovation” (NSRF 2014-2020) and co-financed by Greece and the European Union (European Regional Development Fund). The Finnish Meteorological Institute (FMI) for providing HALO and the NCSRDI for hosting HALO lidar. The authors acknowledge the openair — an R package for air quality data analysis (Carslaw and Ropkins, 2012).

Appendix A. Supplementary data

Supplementary data to this article can be found online at <https://doi.org/10.1016/j.atmosres.2024.107543>.

References

- Amanatidis, G.T., Papadopoulos, K.H., Bartzis, J.G., Helmis, C.G., 1992. Evidence of Katabatic Flows Deduced from a 84 M Meteorological Tower in Athens. *Greece*. Barlow, J.F., Dunbar, T.M., Nemitz, E.G., Wood, C.R., Gallagher, M.W., Davies, F., O’Connor, E., Harrison, R.M., 2011. Boundary layer dynamics over London, UK, as observed using Doppler lidar during REPARTEE-II. *Atmos. Chem. Phys.* 11, 2111–2125. <https://doi.org/10.5194/acp-11-2111-2011>.
- Beddows, D.C.S., Donovan, R.J., Harrison, R.M., Heal, M.R., Kinnersley, R.P., King, M.D., Nicholson, D.H., Thompson, K.C., 2004. Correlations in the chemical composition of rural background atmospheric aerosol in the UK determined in real time using time-of-flight mass spectrometry. *J. Environ. Monit.* 6, 124–133. <https://doi.org/10.1039/B311209H>.
- Beddows, D.C.S., Dell’Osto, M., Harrison, R.M., 2009. Cluster analysis of rural, urban, and curbside atmospheric particle size data. *Environ. Sci. Technol.* 43, 4694–4700. <https://doi.org/10.1021/ES803121T> [SUPPL FILE/ES803121T_SI_001.PDF](https://doi.org/10.1021/ES803121T_SI_001.PDF).
- Bell, M.L., Ebisu, K., Peng, R.D., Samet, J.M., Dominici, F., 2009. Hospital admissions and chemical composition of fine particle air pollution. *Am. J. Respir. Crit. Care Med.* 179, 1115–1120. <https://doi.org/10.1164/RCCM.200808-1240OC>.
- Bousiotis, D., Brean, J., Pope, F.D., Dell’Osto, M., Querol, X., Alastuey, A., Perez, N., Petäjä, T., Massling, A., Neogaard, J.K., Nordström, C., Kouvarakis, G., Vratolis, S., Eleftheriadis, K., Niemi, J.V., Portin, H., Wiedensohler, A., Weinhold, K., Merkel, M., Tuch, T., Harrison, R.M., 2021. The effect of meteorological conditions and atmospheric composition in the occurrence and development of new particle formation (NPFF) events in Europe. *Atmos. Chem. Phys.* 21, 3345–3370. <https://doi.org/10.5194/acp-21-3345-2021>.
- Brook, R.D., Rajagopalan, S., Pope, C.A., Brook, J.R., Bhatnagar, A., Diez-Roux, A., Holguin, F., Hong, Y., Luepker, R.V., Mittleman, M.A., Peters, A., Siscovich, D., Smith, S.C., Whitsel, L., Kaufman, J.D., 2010. Particulate matter air pollution and cardiovascular disease: an update to the scientific statement from the american heart association. *Circulation* 121, 2331–2378. <https://doi.org/10.1161/CIR.0B013E3181DBECE1>.
- Browning, K.A., Wexler, R., 1968. The determination of kinematic properties of a wind field using Doppler radar. *J. Appl. Meteorol.* 7, 105–113. [https://doi.org/10.1175/1520-0450\(1968\)007<0105:TDDKPO>2.0.CO;2](https://doi.org/10.1175/1520-0450(1968)007<0105:TDDKPO>2.0.CO;2).
- Budisulistiorini, S.H., Canagaratna, M.R., Croteau, P.L., Baumann, K., Edgerton, E.S., Kollman, M.S., Ng, N.L., Verma, V., Shaw, S.L., Knipping, E.M., Worsnop, D.R., Jayne, J.T., Weber, R.J., Surratt, J.D., 2014. Intercomparison of an Aerosol Chemical Speciation Monitor (ACSM) with ambient fine aerosol measurements in downtown Atlanta, Georgia. *Atmos. Meas. Tech.* 7, 1929–1941. <https://doi.org/10.5194/amt-7-1929-2014>.
- Carslaw, D.C., Beavers, S.D., 2013. Characterising and understanding emission sources using bivariate polar plots and k-means clustering. *Environ. Model. Softw.* 40, 325–329. <https://doi.org/10.1016/J.ENVSOFT.2012.09.005>.
- Carslaw, D.C., Ropkins, K., 2012. Openair — an R package for air quality data analysis. *Environ. Model. Softw.* 27–28, 52–61. <https://doi.org/10.1016/j.envsoft.2011.09.008>.
- Carslaw, D.C., Beavers, S.D., Ropkins, K., Bell, M.C., 2006. Detecting and quantifying aircraft and other on-airport contributions to ambient nitrogen oxides in the vicinity of a large international airport. *Atmos. Environ.* 40, 5424–5434. <https://doi.org/10.1016/J.ATMOSENV.2006.04.062>.
- Caya, D., Zawadzki, I., 1992. VAD analysis of nonlinear wind fields. *J. Atmos. Ocean. Technol.* 9, 575–587. [https://doi.org/10.1175/1520-0426\(1992\)009<0575:VAONWFS>2.0.CO;2](https://doi.org/10.1175/1520-0426(1992)009<0575:VAONWFS>2.0.CO;2).
- Chalvatzaki, E., Chatzistoudis, S.E., Mammi-Galani, E., Almeida, S.M., Gini, M.I., Eleftheriadis, K., Diapouli, E., Lazaridis, M., 2018. Estimation of the personal deposited dose of particulate matter and particle-bound metals using data from selected European Cities. *Atmosphere* 9 (7), 248. <https://doi.org/10.3390/atmos9070248>.
- Diapouli, E., Popovicheva, O., Kistler, M., Vratolis, S., Persiantseva, N., Timofeev, M., Kasper-Giebel, A., Eleftheriadis, K., 2014. Physicochemical characterization of aged biomass burning aerosol after long-range transport to Greece from large scale wildfires in Russia and surrounding regions, Summer 2010. *Atmos. Environ.* 96, 393–404. <https://doi.org/10.1016/j.atmosenv.2014.07.055>.
- Diapouli, E., Kalogridis, A.C., Markantonaki, C., Vratolis, S., Fetfatzis, P., Colombi, C., Eleftheriadis, K., 2017a. Annual variability of black carbon concentrations originating from biomass and fossil fuel combustion for the suburban aerosol in Athens, Greece. *Atmosphere* 8, 2–234. <https://doi.org/10.3390/ATMOS8120234>.
- Diapouli, E., Manousakas, M.I., Vratolis, S., Vasilatou, V., Pateraki, S., Bairachtari, K.A., Querol, X., Amato, F., Alastuey, A., Karanasiou, A.A., Lucarelli, F., Nava, S., Calzolai, G., Gianelle, V.L., Colombi, C., Alves, C., Custódio, D., Pio, C., Spyrou, C., Kallos, G.B., Eleftheriadis, K., 2017b. AIRUSE-LIFE +: Estimation of natural source contributions to urban ambient air PM10 and PM2.5 concentrations in southern Europe - Implications to compliance with limit values. *Atmos. Chem. Phys.* 17, 3673–3685. <https://doi.org/10.5194/acp-17-3673-2017>.
- Dockery, D.W., Pope, C.A., 1994. Acute respiratory effects of particulate air pollution. *Annu. Rev. Public Health* 15, 107–132. <https://doi.org/10.1146/ANNUREV.PU.15.050194.000543>.
- Eleftheriadis, K., Colbeck, I., Housiadas, C., Lazaridis, M., Mihalopoulos, N., Mitskou, C., Smolik, J., Ždímal, V., 2006. Size distribution, composition and origin of the submicron aerosol in the marine boundary layer during the eastern Mediterranean “SUB-AERO” experiment. *Atmos. Environ.* 40, 6245–6260. <https://doi.org/10.1016/J.ATMOSENV.2006.03.059>.
- Eleftheriadis, K., Ochsenkuhn, K.M., Lymeropoulou, T., Karanasiou, A., Razos, P., Ochsenkuhn-Petropoulou, M., 2014. Influence of local and regional sources on the observed spatial and temporal variability of size resolved atmospheric aerosol mass concentrations and water-soluble species in the Athens metropolitan area. *Atmos. Environ.* 97, 252–261. <https://doi.org/10.1016/J.ATMOSENV.2014.08.013>.
- Eleftheriadis, K., Gini, M.I., Diapouli, E., Vratolis, S., Vefatatzis, P., Manousakas, M.I., 2021. Aerosol microphysics and chemistry reveal the COVID19 lockdown impact on urban air quality. *Sci. Rep.* 11, 1–11. <https://doi.org/10.1038/s41598-021-93650-6>.
- Flocas, H.A., Helmis, C.G., Blikas, S.N., Asimakopoulos, D.N., Bartzis, J.G., Deligiorgi, D.G., 1998. Mean Characteristics of the Katabatic Flow of a 1024m High Knife Edge Mountain. *Theor. Appl. Climatol.* 59 (3), 237–249. <https://doi.org/10.1007/S007040050027>.
- Fröhlich, R., Cubison, M.J., Slowik, J.G., Bukowiecki, N., Prévôt, A.S.H., Baltensperger, U., Schneider, J., Kimmel, J.R., Gomis, M., Rohner, U., Worsnop, D.R., Jayne, J.T., 2013. The ToF-ACSM: a portable aerosol chemical speciation monitor with ToFMS detection. *Atmos. Meas. Tech.* 6, 3225–3241. <https://doi.org/10.5194/amt-6-3225-2013>.
- Gini, M., Manousakas, M., Karydas, A.G., Eleftheriadis, K., 2022. Mass size distributions, composition and dose estimates of particulate matter in Saharan dust outbreaks. *Environ. Pollut.* 298 <https://doi.org/10.1016/J.ENVPOL.2021.118768>.
- Hanna, S.R., Briggs, G.A., Hosker Jr., R.P., 1982. Handbook on Atmospheric Diffusion. <https://doi.org/10.2172/5591108>.
- Henderson, S.W., Gatt, P., Rees, D., Huffaker, R.M., 2005. Wind Lidar. In: Fujii and Fukuchi (Ed.), *Laser Remote Sensing*. CRC Press, Taylor and Francis Group, Boca Raton, FL, pp. 469–722.
- Jiang, Y., Xin, J., Wang, Z., Tian, Y., Tang, G., Ren, Y., Wu, L., Pan, X., Wang, Y., Jia, D., Ma, Y., Wang, L., 2022. The dynamic multi-box algorithm of atmospheric environmental capacity. *Sci. Total Environ.* 806, 150951 <https://doi.org/10.1016/J.SCITOTENV.2021.150951>.
- Kaimal, J.C., Wyngaard, J.C., Haugen, D.A., Coté, O.R., Izumi, Y., Caughey, S.J., Readings, C.J., 1976. Turbulence Structure in the Convective Boundary Layer. *J. Atmos. Sci.* 33, 2152–2169. [https://doi.org/10.1175/1520-0469\(1976\)033<2152:TSITCB>2.0.CO;2](https://doi.org/10.1175/1520-0469(1976)033<2152:TSITCB>2.0.CO;2).
- Kalabokas, P., Viras, L., Repapis, C., 1999. Analysis of the 11-year Record (1987–1997) of Air Pollution measurements in Athens, Greece. Part I: primary air pollutants. *Global NEST J.* 1, 157–167. <https://doi.org/10.30955/GNJ.000135>.
- Kallos, George, Kassomenos, P., Pielke, R.A., 1993. Synoptic and mesoscale weather conditions during air pollution episodes in Athens, Greece. *Bound.-Layer Meteorol.* 62, 163–184. <https://doi.org/10.1007/BF00705553/METRICS>.
- Kalogridis, A.-C., Vratolis, S., Liakou, E., Gerasopoulos, E., Mihalopoulos, N., Eleftheriadis, K., 2018. Assessment of wood burning versus fossil fuel contribution to wintertime black carbon and carbon monoxide concentrations in Athens, Greece. *Atmos. Chem. Phys.* 18, 10219–10236. <https://doi.org/10.5194/acp-18-10219-2018>.
- Katsoulis, B.D., 1996. The relationship between synoptic, mesoscale and microscale meteorological parameters during poor air quality events in Athens, Greece. *Sci. Total Environ.* 181, 13–24. [https://doi.org/10.1016/0048-9697\(95\)04953-3](https://doi.org/10.1016/0048-9697(95)04953-3).
- Kokalis, P., Alexiou, D., Papayannis, A., Rocadenbosch, F., Soupioua, O., Raptis, P.-I., Mylonaki, M., Tzanis, C.G., Christodoulakis, J., 2020. Application and testing of the extended-Kalman-filtering technique for determining the planetary boundary-layer height over athens, Greece. *Bound.-Layer Meteorol.* 176, 125–147. <https://doi.org/10.1007/s10546-020-00514-z>.
- Kostenidou, E., Florou, K., Kaltsonoudis, C., Tsiflikiotou, M., Vratolis, S., Eleftheriadis, K., Pandis, S.N., 2015. Sources and chemical characterization of organic aerosol during the summer in the eastern Mediterranean. *Atmos. Chem. Phys.* 15, 11355–11371. <https://doi.org/10.5194/ACP-15-11355-2015>.
- Laden, F., Schwartz, J., Speizer, F.E., Dockery, D.W., 2006. Reduction in fine particulate air pollution and mortality: Extended follow-up of the Harvard six Cities study. *Am. J. Respir. Crit. Care Med.* 173, 667–672. <https://doi.org/10.1164/RCCM.200503-443OC>.
- Laj, P., 2024. Aerosol, Clouds and Trace Gases Research Infrastructure – ACTRIS, the European research infrastructure supporting atmospheric science. *Bulletin of the American Meteorological Society*. <https://doi.org/10.1175/BAMS-D-23-0064.1>.
- Lelieveld, J., Pozzer, A., Pöschl, U., Fnais, M., Haines, A., Münnel, T., 2020. Loss of life expectancy from air pollution compared to other risk factors: a worldwide perspective. *Cardiovasc. Res.* 116, 1910–1917. <https://doi.org/10.1093/CVR/CVAA025>.

- Li, N., Sioutas, C., Cho, A., Schmitz, D., Misra, C., Sempf, J., Wang, M., Oberley, T., Froines, J., Nel, A., 2003. Ultrafine particulate pollutants induce oxidative stress and mitochondrial damage. *Environ. Health Perspect.* 111, 455–460. <https://doi.org/10.1289/ehp.6000>.
- Liu, C., Chen, R., Sera, F., Vicedo-Cabrera, A.M., Guo, Y., Tong, S., Coelho, M.S.Z.S., Saldiva, P.H.N., Lavigne, E., Matus, P., Valdes Ortega, N., Osorio Garcia, S., Pascal, M., Stafoggia, M., Scorticini, M., Hashizume, M., Honda, Y., Hurtado-Díaz, M., Cruz, J., Nunes, B., Teixeira, J.P., Kim, H., Tobias, A., Íñiguez, C., Forsberg, B., Åström, C., Ragettli, M.S., Guo, Y.-L., Chen, B.-Y., Bell, M.L., Wright, C. Y., Scovronick, N., Garland, R.M., Milojevic, A., Kyselý, J., Urban, A., Orru, H., Indermitte, E., Jaakkola, J.J.K., Ryti, N.R.I., Katsouyanni, K., Analitis, A., Zanobetti, A., Schwartz, J., Chen, J., Wu, T., Cohen, A., Gasparri, A., Kan, H., 2019. Ambient particulate air pollution and daily mortality in 652 Cities. *N. Engl. J. Med.* 381, 705–715. <https://doi.org/10.1056/NEJMoa1817364> DISCLOSURES.PDF.
- Newson, R., Krishnamurthy, R., 2020. Doppler Lidar (DL) Instrument Handbook. PNNL, Richland, WA. <https://doi.org/10.2172/1034640>.
- Olstrup, H., Johansson, C., Forsberg, B., Åström, C., 2019. Association between mortality and short-term exposure to particles, ozone and nitrogen dioxide in Stockholm, Sweden. *Int. J. Environ. Res. Public Health* 16, 1028. <https://doi.org/10.3390/IJERPH16061028>.
- Ostro, B., Broadwin, R., Green, S., Feng, W.Y., Lipsett, M., 2006. Fine particulate air pollution and mortality in nine California Counties: results from calfine. *Environ. Health Perspect.* 114, 29–33. <https://doi.org/10.1289/EHP.8335>.
- Papanikolaou, C.-A., Papayannis, A., Mylonaki, F., Foskinis, R., Kokkalis, P., Liakakou, E., Stavroulas, I., Soupiona, O., Hatzianastassiou, N., Gavrouzou, M., Kralli, E., Anagnou, D., 2022. Vertical profiling of fresh biomass burning aerosol optical properties over the Greek Urban City of Ioannina, during the PANACEA Winter Campaign. *Atmosphere (Basel)* 13, 94. <https://doi.org/10.3390/atmos13010094>.
- Papayannis, A., Balis, D., 1998. Study of the structure of the lower troposphere over Athens using a backscattering Lidar during the MEDCAPHOT-TRACE experiment: measurements over a suburban area. *Atmos. Environ.* 32, 2161–2172.
- Pearson, G., Davies, F., Collier, C., 2010. Remote sensing of the tropical rain forest boundary layer using pulsed Doppler lidar. *Atmos. Chem. Phys.* 10, 5891–5901. <https://doi.org/10.5194/acp-10-5891-2010>.
- Petzold, A., Ogren, J.A., Fiebig, M., Laj, P., Li, S.M., Baltensperger, U., Holzer-Popp, T., Kinne, S., Pappalardo, G., Sugimoto, N., Wehrli, C., Wiedensohler, A., Zhang, X.Y., 2013. Recommendations for reporting black carbon measurements. *Atmos. Chem. Phys.* 13, 8365–8379. <https://doi.org/10.5194/acp-13-8365-2013>.
- Ptaud, J.-P., Pisani, E., Mangold, A., Hueglin, C., Sciaire, J., Pikridas, M., Savvides, C., Ondracek, J., Mbengue, S., Wiedensohler, A., Weinhold, K., Merkel, M., Poulain, L., van Pinxteren, D., Herrmann, H., Massling, A., Nordstroem, C., Alastuey, A., Reche, C., Pérez, N., Castillo, S., Sorribas, M., Adame, J.A., Petaja, T., Lehtipalo, K., Niemi, J., Riffault, V., de Brito, J.F., Colette, A., Favez, O., Petit, J.-E., Gros, V., Gini, M.I., Vratolis, S., Eleftheriadis, K., Diapouli, E., Denier van der Gon, H., Yttri, K. E., Aas, W., 2023. Impact of 2020 COVID-19 lockdowns on particulate air pollution across Europe. *Atmos. Chem. Phys.* 23 (10145–10161) <https://doi.org/10.5194/acp-23-10145-2023>.
- Rousseeuw, P.J., 1987. Silhouettes: a graphical aid to the interpretation and validation of cluster analysis. *J. Comput. Appl. Math.* 20, 53–65. [https://doi.org/10.1016/0377-0427\(87\)90125-7](https://doi.org/10.1016/0377-0427(87)90125-7).
- Salma, I., Balásházy, I., Winkler-Heil, R., Hofmann, W., Záray, G., 2002. Effect of particle mass size distribution on the deposition of aerosols in the human respiratory system. *J. Aerosol Sci.* 33, 119–132. [https://doi.org/10.1016/S0021-8502\(01\)00154-9](https://doi.org/10.1016/S0021-8502(01)00154-9).
- Schween, J.H., Hirsikko, A., Löhner, U., Crewell, S., 2014. Mixing-layer height retrieval with ceilometer and Doppler lidar: from case studies to long-term assessment. *Atmos. Meas. Tech.* 7, 3685–3704. <https://doi.org/10.5194/amt-7-3685-2014>.
- Seinfeld, J.H., Pandis, S.N., 2016. *Atmospheric Chemistry and Physics: From Air Pollution to Climate Change*, 3rd Edition, ISBN: 978-1-118-94740-1. Wiley, New Jersey.
- Soupiona, O., Samaras, S., Ortiz-Amezcua, P., Böckmann, C., Papayannis, A., Moreira, G. A., Benavent-Oltra, J.A., Guerrero-Rascado, J.L., Bedoya-Velásquez, A.E., Olmo, F.J., Román, R., Kokkalis, P., Mylonaki, M., Alados-Arboledas, L., Papanikolaou, C.A., Foskinis, R., 2019. Retrieval of optical and microphysical properties of transported Saharan dust over Athens and Granada based on multi-wavelength Raman lidar measurements: Study of the mixing processes. *Atmos. Environ.* 214, 116824 <https://doi.org/10.1016/J.ATMOSENV.2019.116824>.
- Stafoggia, M., Schneider, A., Cyrys, J., Samoli, E., Andersen, Z.J., Bedada, G.B., Bellander, T., Cattani, G., Eleftheriadis, K., Faustini, A., Hoffmann, B., Jacquemin, B., Katsouyanni, K., Massling, A., Pekkanen, J., Perez, N., Peters, A., Quass, U., Yli-Tuomi, T., Forastiere, F., 2017. Association between short-term exposure to ultrafine particles and mortality in eight European urban areas. *Epidemiology* 28, 172–180. <https://doi.org/10.1097/EDE.0000000000000599>.
- Stull, R.B., 1988. An introduction to boundary layer meteorology. In: *An Introduction to Boundary Layer Meteorology*. <https://doi.org/10.1007/978-94-009-3027-8>.
- Su, T., Li, Z., Kahn, R., 2018. Relationships between the planetary boundary layer height and surface pollutants derived from lidar observations over China: regional pattern and influencing factors. *Atmos. Chem. Phys.* 18, 15921–15935. <https://doi.org/10.5194/acp-18-15921-2018>.
- Träumner, K., Kottmeier, C., Corsmeier, U., Wieser, A., 2011. Convective Boundary-Layer Entrainment: Short Review and Progress using Doppler Lidar. *Bound.-Layer Meteorol.* 141 (3), 369–391. <https://doi.org/10.1007/S10546-011-9657-6>.
- Tucker, S.C., Brewer, W.A., Banta, R.M., Senff, C.J., Sandberg, S.P., Law, D.C., Weickmann, A.M., Hardesty, R.M., 2009. Doppler lidar estimation of mixing height using turbulence, shear, and aerosol profiles. *J. Atmos. Ocean. Technol.* 26, 673–688. <https://doi.org/10.1175/2008JTECHA1157.1>.
- Vratolis, S., Gini, M.I., Bezantakos, S., Stavroulas, I., Kalivitis, N., Kostenidou, E., Louvaris, E., Siakavaras, D., Biskos, G., Mihalopoulos, N., Pandis, S.N., Pilinis, C., Papayannis, A., Eleftheriadis, K., 2019. Particle number size distribution statistics at City-Centre Urban Background, urban background, and remote stations in Greece during summer. *Atmos. Environ.* 213, 711–726. <https://doi.org/10.1016/j.atmosenv.2019.05.064>.
- Vratolis, S., Fettatidis, P., Argyrouli, A., Soupiona, O., Mylonaki, M., Maroufidis, J., Kalogridis, A.-C., Manousakas, M., Bezantakos, S., Binietoglou, I., Labzovskii, L.D., Solomos, S., Papayannis, A., Moćnik, G., O'Connor, E., Müller, D., Tzanis, C.G., Eleftheriadis, K., 2020. Comparison and Complementary Use of In Situ and Remote Sensing Aerosol Measurements in the Athens Metropolitan Area Atmospheric Environment, p. 228. <https://doi.org/10.1016/j.atmosenv.2020.117439>.
- Wiedensohler, A., Birmili, W., Nowak, A., Sonntag, A., Weinhold, K., Merkel, M., Wehner, B., Tuch, T., Pfeifer, S., Fiebig, M., Fjärraa, A.M., Asmi, E., Sellegrí, K., Depuy, R., Venzac, H., Villani, P., Laj, P., Aalto, P., Ogren, J.A., Swietlicki, E., Williams, P., Roldin, P., Quincey, P., Hüglin, C., Fierz-Schmidhauser, R., Gysel, M., Weingartner, E., Riccobono, F., Santos, S., Griniung, C., Faloon, K., Beddows, D., Harrison, R., Monahan, C., Jennings, S.G., O'Dowd, C.D., Marinoni, A., Horn, H.-G., Keck, L., Jiang, J., Scheckman, J., McMurry, P.H., Deng, Z., Zhao, C.S., Moerman, M., Henzing, B., de Leeuw, G., Löschau, G., Bastian, S., 2012. Mobility particle size spectrometers: harmonization of technical standards and data structure to facilitate high quality long-term observations of atmospheric particle number size distributions. *Atmos. Meas. Tech.* 5, 657–685. <https://doi.org/10.5194/amt-5-657-2012>.
- WMO, 2022. *WMO Greenhouse Gas Bulletin. No. 2, September 2022. World Meteorological Organization (WMO)*.
- Zografou, O., Gini, M., Manousakas, M.I., Chen, G., Kalogridis, A.C., Diapouli, E., Pappa, A., Eleftheriadis, K., 2022. Combined organic and inorganic source apportionment on yearlong ToF-ACSM dataset at a suburban station in Athens. *Atmos. Meas. Tech.* 15, 4675–4692. <https://doi.org/10.5194/AMT-15-4675-2022>.